Innovative ochre processing and tool use in China 40,000 years ago

Fa-Gang Wang, Shi-Xia Yang, Jun-Yi Ge, Andreu Ollé, Ke-Liang Zhao, Jian-Ping Yue, Daniela Eugenia Rosso, Katerina Douka, Ying Guan, Wen-Yan Li, et al.

To cite this article, please quote:" Wang, FG., Yang, SX., Ge, JY. *et al.* Innovative ochre processing and tool use in China 40,000 years ago. *Nature* 603, 284–289 (2022). https://doi.org/10.1038/s41586-022-04445-2"

Innovative ochre processing and tool use in China ~40,000 years ago

Fa-Gang Wang[1]†, Shi-Xia Yang[2,3,4,5]†* Jun-Yi Ge[2,3], Andreu Ollé[6,7], Ke-Liang Zhao[2,3], Jian-Ping Yue[8], Daniela Eugenia Rosso[9,10], Katerina Douka[4,11], Ying Guan[2,3], Wen-Yan Li[1], Hai-Yong Yang[12], Lian-Qiang Liu[1], Fei Xie[1], Zheng-Tang Guo[13], Ri-Xiang Zhu[14], Cheng-Long Deng[14,15]*, Francesco d'Errico[16,17]*, Michael Petraglia[4,18,19,20]*

[1]Hebei Provincial Institute of Cultural Relics and Archeology, Shijiazhuang 050031, China.
[2]Key Laboratory of Vertebrate Evolution and Human Origins, Institute of Vertebrate Palaeontology and Palaeoanthropology, Chinese Academy of Sciences, Beijing 100044, China.
[3]Center for Excellence in Life and Palaeoenvironment, Chinese Academy of Sciences, Beijing 100044, China.
[4]Department of Archaeology, Max Planck Institute for the Science of Human History, Jena 07745, Germany.
[5]State Key Laboratory of Loess and Quaternary Geology, Institute of Earth Environment, Chinese Academy of Sciences, Xi'an 710061, China.
[6]Institut Català de Palaeoecologia Humana i Evolució Social (IPHES-CERCA), Zona Educacional 4, Campus Sescelades URV (Edifici W3), 43007, Tarragona, Spain.
[7]Universitat Rovira i Virgili, Dept. d'Història i Història de l'Art, Av. Catalunya 35, 43002, Tarragona, Spain.
[8]Department of History, Anhui University, Hefei 230039, China.
[9]Université Côte d'Azur, CNRS, CEPAM, Nice, France.
[10]Departament de Prehistòria, Arqueologia i Història Antiga, Grupo de Investigación Prehistoria del Mediterráneo Occidental (PREMEDOC), Universitat de València, Valencia, Spain.
[11]Oxford Radiocarbon Accelerator Unit, Research Laboratory for Archaeology and the History of Art, University of Oxford, Oxford, OX1 3TG, UK.
[12]Museum of Yuzhou, Yuxian 075700, China.
[13]Key Laboratory of Cenozoic Geology and Environment, Institute of Geology and Geophysics, Chinese Academy of Sciences, Beijing 100029, China.
[14]State Key Laboratory of Lithospheric Evolution, Institute of Geology and Geophysics, Chinese Academy of Sciences, Beijing 100029, China.
[15]College of Earth and Planetary Sciences, University of Chinese Academy of Sciences, Beijing 100049, China.
[16]PACEA UMR 5199, Université de Bordeaux, CNRS, Pessac, France.
[17]SFF Centre for Early Sapiens Behaviour (SapienCE), University of Bergen, Bergen, Norway.
[18]Human Origins Program, National Museum of Natural History, Smithsonian Institution, Washington, D.C. 20560, USA.
[19]School of Social Science, The University of Queensland, Brisbane, Queensland 4072, Australia.
[20]Australian Research Centre for Human Evolution (ARCHE), Griffith University, Brisbane, Australia.

†These authors contributed equally to this work.
* Corresponding authors. yangshixia@ivpp.ac.cn (S.X.Y.), cldeng@mail.iggcas.ac.cn (C.L.D.), francesco.derrico@u-bordeaux.fr (F.D.), petraglia@shh.mpg.de (M.P.).

Homo sapiens was present in northern Asia by ~40,000 years ago, having ultimately replaced archaic populations in Eurasia after episodes of earlier population expansions and interbreeding[1–4]. Cultural adaptations associated with the last Neanderthals, Denisovans and the incoming populations of *H. sapiens* into Asia remain elusive[1,5–7]. Here, we describe Xiamabei, a well-preserved, ~40,000-year-old archaeological site in northern China, containing the earliest known ochre processing feature in Eastern Asia together with a distinctive miniaturized lithic assemblage, with bladelet-like tools bearing traces of hafting, and a bone tool. The cultural assembly of traits at Xiamabei is unique for Eastern Asia and does not correspond with those found at other archaeological site assemblages inhabited by archaic populations or to those generally associated with the expansion of *H. sapiens*, such as the Initial Upper Palaeolithic[8–10]. The record of northern Asia supports a process of cultural diversification and innovations emerging in a period of hominin hybridization and admixture[2,6,7,11].

Main Text

One of the most profound events in human evolution was the worldwide expansion of *Homo sapiens*[1,5,12]. Fossil, genetic and archaeological evidence indicates that *H. sapiens* dispersed out of Africa multiple times over the last ~200 thousand years (ka)[1,13], interbreeding with archaic hominins, such as the Neanderthals and Denisovans as they migrated across Eurasia[6,8,14]. Current palaeoanthropological and archaeological evidence demonstrates that *H. sapiens* was present in northern Asia by at least 40 ka ago[2–4]. It is often argued that the terrestrial expansion of modern humans was facilitated by the use of advanced economic, social and symbolic adaptations allowing occupation of a variety of ecosystems[14]. Pigment use, in particular, is seen as a key indicator of symbolically mediated behaviour[15–17], and technological innovations, such as the use of miniturised technology, is considered to have had adaptive and economic advantages[18,19]. Archaeological data, however, remain ambiguous as to the arrival of *H. sapiens* populations in China (Supplementary Information A). With the exception of Initial Upper Palaeolithic (IUP) and Mousterian toolkits in the Altai and Siberia, and a few sites in northern China[20–22], little is

known about stone tool industries in Eastern Asia until microblade assemblages become the dominant technology after 29 ka[9,23,24]. With respect to possible evidence for early symbolism, only two engraved bones are known, one bearing residues of ochre, from northern China (ca. 125–105 ka), interpreted as the product of archaic hominins[25]. Most artefacts signaling symbolic practices are much younger, and likely linked to *H. sapiens*, such as pendants and ochre at Zhoukoudian Upper Cave (ca. 35.1–33.5 ka)[4] and beads at Shuidonggou 2 (SDG 2) (ca. 31 ka)[23]. Beads, pendants, and figurines become common after ca. 29 ka, when microblade technology began to spread across northern China[26–28].

Here we report the results of archaeological findings at Xiamabei, a newly excavated and well-preserved site in the Nihewan Basin of northern China (Fig. 1). Xiamabei contains the earliest evidence of ochre processing, a novel miniaturized lithic technology, with bladelet-like forms and hafted items, and a bone tool, dating to ~41–39 ka. Xiamabei stands apart from any other known archaeological site in China as it possesses a novel set of cultural characteristics at an early date. Located at the transition zone between the Inner Mongolian Plateau and North China Plain, the site offers important new insights in the expansion of *H. sapiens* along the northern route[10].

Xiamabei is on the southern bank of the Huliu River, where excavations were initiated in 2013 in the form of a trench exposing a 12 m^2 area (Supplementary Information B). The stratigraphy, extending to a depth of 290 cm, encompasses six main layers in a floodplain environment (Fig. 2). Layer 6, the main cultural horizon, 10–20 cm in thickness, is composed of dark brown silty sediment, with occasional clay and sand aggregates. Layer 6 revealed evidence for ochre use and processing, a charcoal-rich hearth, 382 miniaturized lithics, a single bone tool (Extended Data Fig. 1) and 437 mammal bones (Fig. 1b–d). Characterization methods were applied to sediment samples, ochre items, the bone tool, and a sample of the miniaturized lithics. Accelerator mass spectrometry (AMS) ^{14}C and optically stimulated luminescence (OSL) dating yielded ages ranging between ca. 43 ka to 28 ka for the sequence, with the Layer 6 cultural horizon dating to ca. 41–39 ka (Fig. 2, Supplementary Information C).

Pollen from Layer 6 indicates a steppe landscape with patches of coniferous forest dominated by *Pinus*. The pollen assemblages and high *Artemisia*/Chenopodiaceae (A/C) ratio in Layer 6 indicate a relatively cool and semi-arid climate during the site occupation (Supplementary Information D). Faunal remains were highly fragmentary, with only 7.19%

being taxonomically identifiable. The presence of horse, deer and zokor is consistent with the pollen evidence, reflecting a steppe landscape with patches of forest (Supplementary Information D). The bulk of the mammalian fossils were less than 20 mm in length and most were burnt, some even highly carbonized, suggesting their possible use as fuel (Supplementary Information D2). Cutmarks were identified on two faunal fragments indicating that lithics were used to process carcasses. A single bone tool bearing traces of use wear in the form of microflake scars and polishing at one end, and regularization by scraping at the other end, possibly to facilitate prehension or hafting, was recovered from Layer 6. The tool represents one of the earliest examples in northern China for the working of bone with techniques proper to this raw material (Extended Data Fig. 1).

Ochre processing evidence

Evidence for ochre processing at Xiamabei consists of three artefacts lying in close spatial association and on a spot of red stained sediment whose colouration reduces in intensity on the objects (Fig. 3, Extended Data Figs. 2–5, Supplementary Information E and F). The three artefacts (Figs. 3a, b) consist of an ochre piece (OP1) consisting of an allochthonous hard iron-rich nodule bearing clear traces of having been repeatedly abraded to produce a bright dark red ochre powder (Fig. 3c), a smaller and more friable ochre piece (OP2) of a different composition (Fig. 3d), resulting from crushing an original larger piece to produce ochre powder, and an elongated limestone slab (LS) with smoothed areas stained with ochre (Fig. 3e) and preserving residues of hematite-rich ochre (Fig. 3f) similar to that composing the smaller ochre piece. No ochre residues were identified on an associated quartzite cobble (QC) bearing evidence of use as a pestle (Fig. 3g).

X-ray diffraction (XRD), Micro Raman spectroscopy (MR), Micro-X-ray fluorescence (Micro-XRF), mineral magnetism (MM), scanning electron microscopy coupled with energy dispersive spectroscopy (SEM-EDS) were applied to 12 sediment samples from inside and outside the red stained area on which the ochre pieces and associated artefacts were lying (Extended Data Fig. 6, Supplementary Information G). In contrast to samples located at various distances from the red stained area, two samples from inside the area are rich in FeO and contain abundant microfragments of hematite-rich rocks. This indicates that the reddish colour of the

sediment (on which the stone artefacts and the ochre fragments were laying) is due to the presence of diffuse ochre particles.

Taken together, the evidence indicates that different types of ochre were brought to the site and processed using abrasion and pounding to produce ochre powder of different colour and granulometry. Although the purpose of such an activity cannot be established (e.g., the production of paint for colouring objects or decorating bodies, tanning of hides, using ochre as a loading agent for adhesives), the quantity of ochre powder produced was large enough for the leftover to permanently impregnate the sediment of the area on which tasks took place. This work area, which represents the earliest known instance of ochre processing in Eastern Asia[28], indicates that the use of this material was part of the behavioural repertoire of regional populations by ~40 ka, preceding the origin of microblade technologies in China by 10,000 years.

Novel miniaturized lithic assemblage with hafting evidence

The Xiamabei lithic assemblage, composed of 382 artefacts, is a novel technology for northern China, especially in consideration of its age. Most of the lithic artefacts (94%) are smaller than 40 mm and 58.37% (n=209) are smaller than 20 mm. Locally available small chert nodules and quartz pebbles dominate the lithic assemblage, though porphyry pebbles were also sometimes used. Freehand Hard Hammer Percussion (FHHP) and Bipolar Percussion (BP) methods were the main reduction techniques, as shown by the coexistence of flake-cores with pronounced Hertzian initiations and bipolar pieces with evidence of crushing on opposed platforms and diffuse bulbs of percussion (Supplementary Information H). BP is the predominant reduction technique, contributing to 70.11% of the identifiable specimens. The maximum length and width of BP cores were not significantly smaller than the FHHP cores, indicating that although hand-held flaking of small cores was possible, preference was given to bipolar reduction. Bipolar splinters had an average width of 13.59 mm (29.5% smaller than 10 mm), falling within the width range of formal microblades from younger sites in northern China[29]. BP reduction strategies therefore resulted in the efficient production of bladelet-like blanks that could be used as tools, with lengths frequently measuring 20 mm or less (Fig. 4)[30].

In contrast to both earlier and contemporary lithic assemblages from the Nihewan Basin[31,32] retouched tools are exceedingly rare at Xiamabei. Only three pieces in the Xiamabei assemblage show formal edge modification: two denticulates and one slightly retouched end-

scraper. Functional analysis conducted on a selected sample of lithics, including 13 bipolar and 4 FHHP products, identified use-wear on most of them (Supplementary Information I). Seven pieces show clear evidence of hafting based on the arrangement of micro-scarring, the absence of use-wear on areas covered by the hafting material, and the frequent presence of plant fiber imprints, pointing to the use of binding elements (Fig. 4). Bone hafts have been identified in two cases and exceptionally illustrated by a bladelet-like piece recovered with a portion of the haft still in place (Fig. 4a, Extended Data Figs. 7–9). Wear patterns indicate the hafted pieces were used for a variety of purposes including hide scraping, boring and scraping against hard matter (likely wood), whittling soft plant material, and probably cutting soft animal matter. Two pieces bearing an end-scraper outline were used in a manner consistent with classic Upper Palaeolithic hide working tools, although only one of the implements showed formal distal retouch (Fig. 4b). Use-wear on unhafted pieces complete the range of identified activities - mainly represented by cutting actions on different materials, boring on a hard material, and in two cases, as wedges on quartz flakes. Overall, the microscopic analyses indicated that the Xiamabei artefacts, including bladelet-like tools manufactured by the BP technique, were used in a variety of activities (Extended Data Fig. 10). In addition, ten artefacts with ochre residues, mainly in the form of dispersed particles, were identified. On four pieces, residues were associated with the hafted area, and on two pieces hide working was identified as residues were located on the active edge. Ochre may have been used as an additive for hide working or as a loading agent for a hafting adhesive.

Implications for cultural adaptations in Eastern Asia

The Xiamabei site excavations and analyses identifies the appearance, ~40,000 years ago, of new cultural features that were either unknown or exceedingly rare in this region and in the neighboring regions. The combination of two knapping techniques for the production of small blanks, used for a variety of tasks and sometimes hafted, indicates the existence of a complex technical system involving the use and transformation of different raw materials. Such a technical system, not identified at older and penecontemporaneous sites, gives the Xiamabei assemblage an original character. A workshop for the production and use of mineral pigments at Xiamabei constitutes a second new cultural element in comparison with earlier and contemporary sites. The use of ochre is not, however, associated with ostrich egg beads and

pierced teeth and shells found in younger sites, nor with the arrival, attested at younger sites, of microblade technology. Although the taxonomic affiliation of the human group that occupied Xiamabei ~40,000 years ago is not known, and an occupation by late Denisovans or even Neanderthals cannot be excluded, the most parsimonious hypothesis, considering the presence of contemporary fossils of modern humans at Tianyuandong[2], and somewhat younger at Salkhit[3] and Zhoukoudian Upper Cave[4], is that the visitors to Xiamabei were *H. sapiens*.

The way in which key cultural innovations emerged in different regions of the world remains unclear. For some regions, such as Africa, a discontinuous and regionally variable accretion model has been proposed, indirectly linked to the long and complex process that has led to the emergence of our species in that continent[33]. It has been argued that packages of innovations originally developed in Africa or elsewhere may have been introduced by the spread of modern humans into Eurasia. This is the model most often favoured for Asia, a region in which, following European trends, blade and microblade technology, personal ornaments, ochre use and complex bone technologies are seen as the signature of incoming *H. sapiens* populations.

The record emerging from northern China challenges dominant paradigms by showing that during a critical time window, at ca. 40 ka, a variety of cultural adaptations existed. The occurrence of a varied, though more simple lithic technology when compared to bladelet production, associated with previously unrecorded hafting techniques, and the presence of some innovations (ochre use, an expedient bone tool), and not others (formal bone tools, ornaments), suggest that the cultural adaptations at Xiamabei may reflect a first colonisation by modern humans, potentially involving cultural and genetic mixing with local Denisovans, and perhaps replaced by a later second arrival. This supports the view that current evolutionary scenarios are simplistic and that we should expect repeated but differential episodes of genetic and cultural exchange over large geographic areas. We should also expect to identify a mosaic pattern involving, in some instances, the spread of innovation packages, and in others, the persistence of local traditions or the adoption of local invention of innovations with different rates of complexities in technological and symbolic practices. This more complex evolutionary scenario fits better with current biological and cultural evidence in comparison to one that envisions a spread of innovation associated with a single, rapid wave of *H. sapiens* populations across Eurasia.

References

1. Bae, C. J., Douka, K. & Petraglia, M. On the origin of modern humans: Asian perspectives. *Science* **358**, 1269–1269 (2017).
2. Fu, Q. et al. DNA analysis of an early modern human from Tianyuan Cave, China. *Proc. Natl. Acad. Sci. U.S.A.* **110**, 2223–2227 (2013).
3. Massilani, D. et al. Denisovan ancestry and population history of early East Asians. *Science* **370**, 579–583 (2020).
4. Li, F., Bae, C. J., Ramsey, B., Chen, F. & Gao, X. Re-dating Zhoukoudian Upper Cave, northern China and its regional significance. *J. Hum. Evol.* **121**, 170–177 (2018).
5. Timmermann, A. & Friedrich, T. Late Pleistocene climate drivers of early human migration. *Nature* **538**, 92–95 (2016).
6. Kuhlwilm, M. I. et al. Ancient gene flow from early modern humans into Eastern Neanderthals. *Nature* **530**, 429–433 (2016).
7. Bae, C. J. et al. Late Pleistocene human evolution in Eastern Asia behavioral perspectives. *Curr. Anthropol.* **58**, 514–526 (2017).
8. Hajdinjak, M. et al. Initial Upper Palaeolithic humans in Europe had recent Neanderthal ancestry. *Nature* **592**, 253–257 (2021).
9. Bar-Yosef, O. & Wang, Y. Palaeolithic Archaeology in China. *Annu. Rev. Anthropol.* **41**, 319–335 (2012).
10. Li, F., Petraglia, M., Roberts, P. & Gao, X. The northern dispersal of early modern humans in eastern Eurasia. *Chin. Sci. Bull.* **65**, 1699–1701 (2020).
11. Dennell, R., Martinón-Torres, M., de Castro, J. M. B. & Gao, X. A demographic history of late Pleistocene China. *Quat. Int.* **559**, 4–13 (2020).
12. deMenocal, P. B. & Stringer, C. Climate and the peopling of the world. *Nature* **538**, 49–50 (2016).
13. Harvati, K. et al. Apidima Cave fossils provide earliest evidence of *Homo sapiens* in Eurasia. *Nature* **571**, 500–504 (2019).
14. Dennell, R. *From Arabia to the Pacific: How Our Species Colonised Asia* (Routledge, London, ed. 1, 2020).
15. Hovers, E., Ilani, S., Bar-Yosef, O. & Vandermeersch, B. An early case of color symbolism: ochre use by modern humans in Qafzeh Cave. *Curr. Anthropol.* **44**, 491–522 (2003).
16. Watts, I. Red ochre, body painting, and language: interpreting the Blombos ochre. *The Cradle of Language* **2**, 93–129 (2009).
17. Zipkin, A. M. *Material Symbolism and Ochre Exploitation in Middle Stone Age East-Central Africa* (Doctoral dissertation, The George Washington University, 2015).
18. Villa, P. et al. Border Cave and the beginning of the Later Stone Age in South Africa. *Proc. Natl. Acad. Sci. U.S.A.* **109**, 13208–13213 (2012).
19. Pargeter, J. & Shea, J. Going big versus going small: Lithic miniaturization in hominin lithic technology. *Evol. Anthropol.* **28**, 72–85 (2019).
20. Zwyns, N. et al. The northern route for human dispersal in central and Northeast Asia: New evidence from the site of Tolbor-16, Mongolia. *Sci. Rep.* **9**, 11759 (2019).
21. Peng, F., Lin, S. C., Patania, I. & Levchenko, V. A chronological model for the Late Paleolithic at Shuidonggou Locality 2, North China. *PLoS ONE* **15**, e023268 (2020).
22. Li, F. et al. The easternmost Middle Paleolithic (Mousterian) from Jinsitai Cave, North China. *J. Hum. Evol.* **114**, 76–84 (2018).
23. Li, F. et al. Chronology and techno-typology of the Upper Palaeolithic sequence in the Shuidonggou area, northern China. *J. World Prehistory* **32**, 111–141 (2019).
24. Yue, J. et al. Human adaptations during MIS 2: Evidence from microblade industries of Northeast China. *Palaeogeogr. Palaeoclimatol. Palaeoecol.* **567**, 110286 (2021).
25. Li, Z., Doyon, L., Li, H., Wang, Q. & d'Errico, F. Engraved bones from the archaic hominin site of Lingjing, Henan Province. *Antiquity* **93**, 886–900 (2019).
26. Wei, Y., d'Errico, F., Vanhaeren, M., Peng, F. & Gao, X. A technological and morphological study of Late Paleolithic ostrich eggshell beads from Shuidonggou, North China. *J. Archaeol. Sci.* **85**, 83–104 (2017).
27. Qu, T., Bar-Yosef, O., Wang, Y. & Wu, X. The Chinese Upper Paleolithic: Geography, Chronology, and Techno-typology. *J. Archaeol. Res.* **21**, 1–73 (2013).
28. Martí, A. P., Wei, Y., Gao, X., Chen, F. & d'Errico, F. The earliest evidence of coloured ornaments in China: The ochred ostrich eggshell beads from Shuidonggou Locality 2. *J. Anthropol. Archaeol.* **48**, 102–113 (2017).
29. Guan, Y. et al. Microblade remains from the Xishahe site, North China and their implications for the origin of microblade technology in Northeast Asia. *Quat. Int.* **535**, 38–47 (2020).

30. Pargeter, J. & Faith, T. J. Lithic miniaturization as adaptive strategy: a case study from Boomplaas Cave, South Africa. *Archaeol. Anthrop. Sci.* **12**, 225 (2020).
31. Guo, Y. J. et al. Luminescence ages for three 'Middle Paleolithic' sites in the Nihewan Basin, northern China, and their archaeological and palaeoenvironmental implications. *Quat. Res.* **85**, 456–470 (2016).
32. Yang, S., Deng, C., Zhu, R. & Petraglia, M. The Paleolithic in the Nihewan Basin, China: Evolutionary history of an Early to Late Pleistocene record in Eastern Asia. *Evol. Anthropol.* **29**, 125–142 (2020).
33. Scerri, E., Chikhi, L. & Thomas, M. Beyond multiregional and simple out-of-Africa models of human evolution. *Nat. Ecol. Evol.* **3**, 1–3 (2019).

Acknowledgements

We thank Y. Lefrais (IRAMAT-CRP2A, UMR 5060 CNRS CNRS – Université Bodeaux-Montaigne, France) and F. Orange (Université Côte d'Azur, Centre Commun de Microscopie Appliquée, CCMA, Nice, France) for assistance with SEM-EDS analyses; A. Queffelec (PACEA UMR 5199, University Bordeaux, CNRS, France) and L. Geis (PACEA UMR 5199, University Bordeaux, CNRS, France) for assistance with the EDXRF analyses and the 3D imaging; C. X. Zhang, B. Hu, M. L. Zhou, J. H. Li, Y. Liu, S. H. Yang, X. G. Li, Y. Chen, J. Yuan, Z. S. Shen, S. Zhang and Z. X. Jiang (Institute of Geology and Geophysics, Chinese Academy of Sciences) for assistance with the sediment analysis; B. Xu (Institute of Geology and Geophysics, Chinese Academy of Sciences) and Y. Li (China University of Geosciences, Beijing) for discussions on dating results; and R. P. Tang and F. X. Huan (Institute of Vertebrate Palaeontology and Palaeoanthropology, Chinese Academy of Sciences) for assistance with figure preparation.

Funding Financial support for this research was provided by the National Natural Science Foundation of China (41888101, 42177424, 41977380, 42072212 and 41690112), the Strategic Priority Research Program of Chinese Academy of Sciences (XDB26000000), the Key Research Program of the Institute of Geology & Geophysics, Chinese Academy of Sciences (IGGCAS-201905), the State Key Laboratory of Loess and Quaternary Geology, Institute of Earth Environment (SKLLQGZR2002), the Youth Innovation Promotion Association of Chinese Academy of Sciences (2020074), the Humboldt Foundation, and the Max Planck Society. O.A. was supported by the Spanish MICIU/Feder (PGC2018-093925-B-C32), the Catalan AGAUR (SGR2017-1040) and the Univ. Rovira i Virgili (2019-PFR-URV-91) in the context of a MICIN "María de Maeztu" excellence accreditation (CEX2019-000945). D.E.R. was funded by the Fyssen Foundation, France, and the Juan de la Cierva-Formación Research Fellowship (FJC2018-035605-I; Ministerio de Ciencia e Innovación, Spain). F.D. was funded by the Research Council of Norway through its Centre of Excellence funding scheme (SFF Centre for Early Sapiens Behaviour –SapienCE– project number 262618), the Talents program and the GPR Human Past of the University of Bordeaux Initiative of Excellence. KD has received funding from the ERC under the European Union's Horizon 2020 research and innovation program, grant agreement 715069-FINDER-ERC-2016-STG.

Author contributions F.G.W., S.X.Y., C.L.D, R.X.Z., Z.T.G., F.D.E. and M.P. obtained funding and initiated the project; F.G.W., S.X.Y., J.Y.G, L.Q.L., F.X., Y. H.Y.,Y.G. and W.Y.L.

conducted field excavation and site sampling; J.Y.G., K.L.Z., K.D. and C.L.D. conducted stratigraphic and palaeoenvironmental studies; J.Y.G. performed the OSL dating; K.D. performed the ^{14}C dating; S.X.Y., J.P.Y., M.P. and A.O. analyzed the stone artefacts; F.D.E., D.E.R., Y.G. and C.L.D. analyzed the ochre processing artefacts and the sediment; and S.X.Y., C.L.D, F.D.E. and M.P wrote the main text and supplementary materials with specialist contributions from the other authors.

Competing interests The authors declare no competing interests.

Data and materials availability All relevant data are available in the main text or the accompanying supplementary materials. All artefacts referred to in this study are curated in the Institute of Vertebrate Palaeontology and Palaeoanthropology, Chinese Academy of Sciences, Beijing, and Hebei Provincial Institute of Cultural Relics and Archeology in Shijiazhuang, China. They are available for further research.

Supplementary Materials

Supplementary Information A–I

SI References

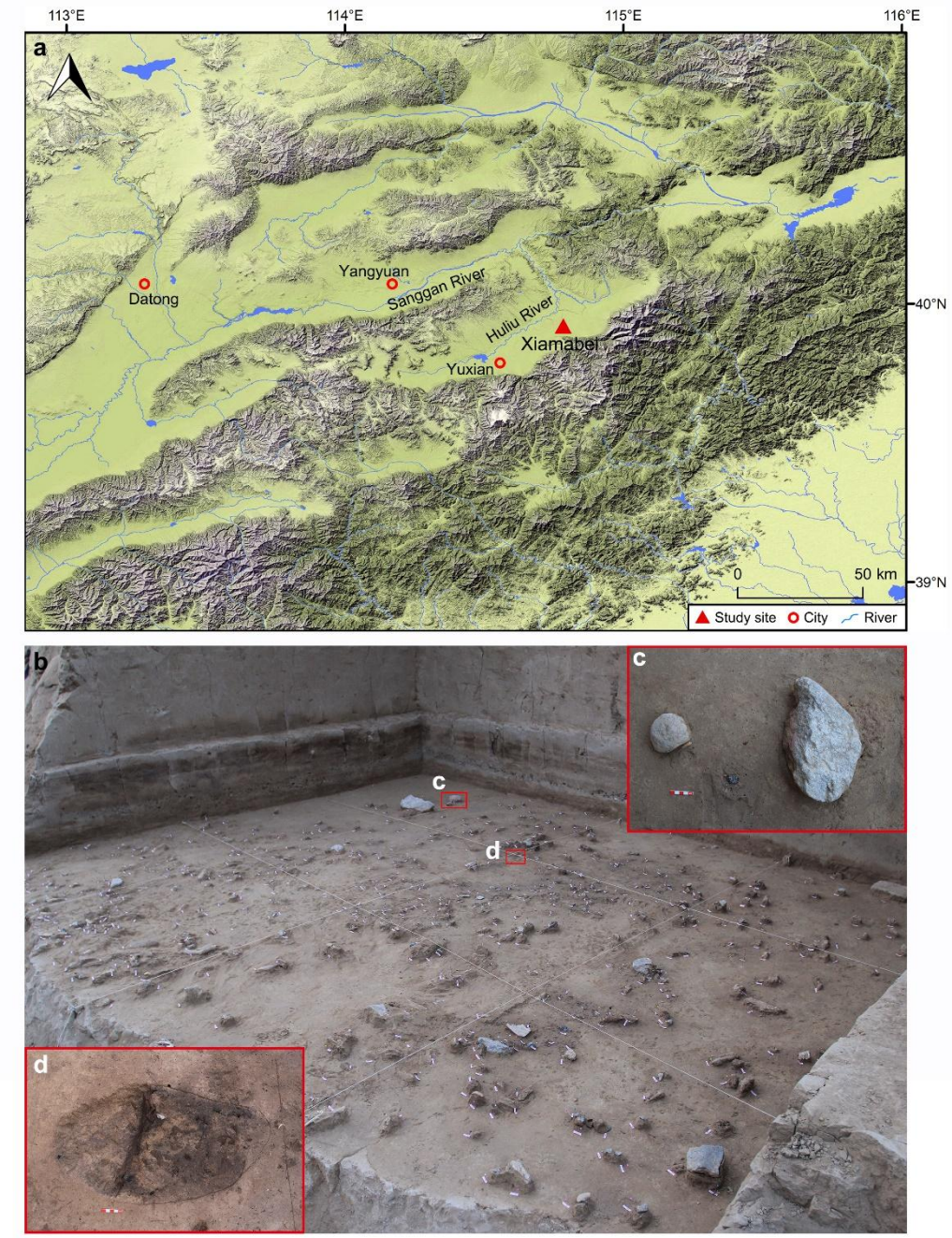

Fig. 1 | Location of Xiamabei in the Nihewan Basin, China, and archaeological site excavations. **a**, Location of Xiamabei in northern China, with regional map showing the location of the site on the south bank of the Huliu River, Nihewan Basin. **b**, Distribution of cultural remains on the Layer 6 surface. **c**, Ochre processing feature showing a quartzite cobble (QC), an ochre piece (OP1) and a limestone slab (LS). **d**, View of the Layer 6 hearth, dated to ~41–39 ka.

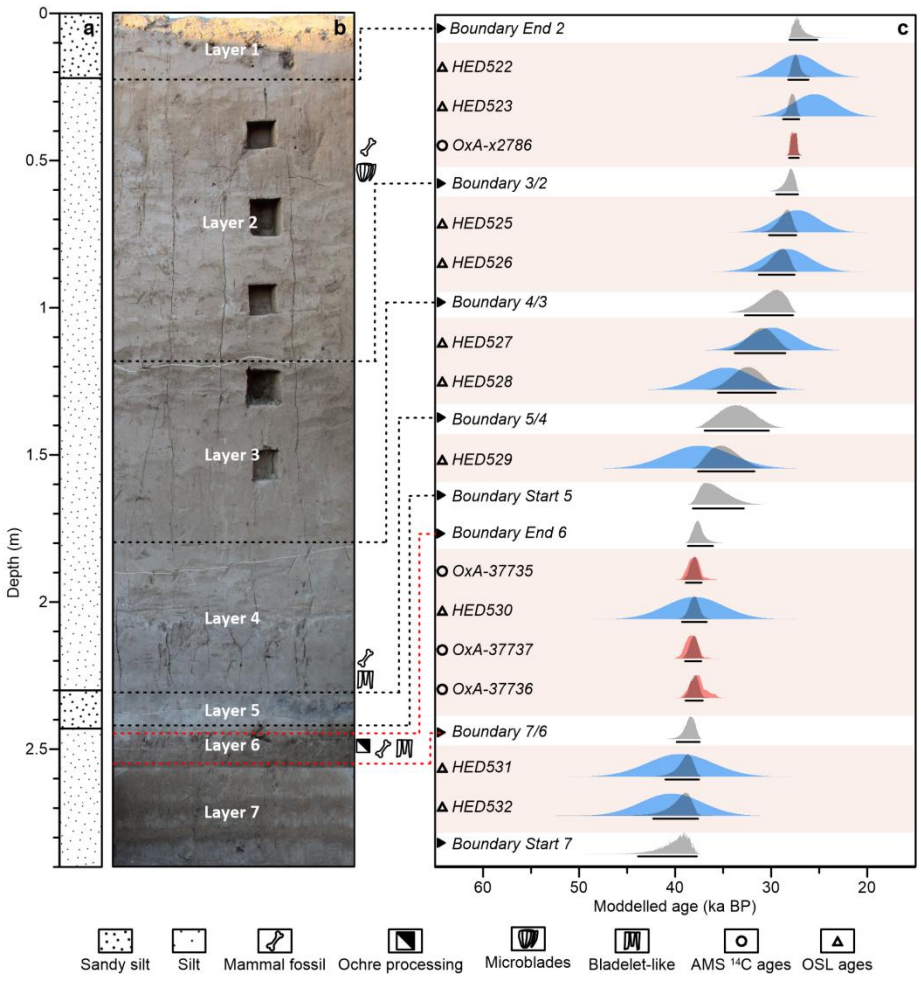

348

349 **Fig. 2 | Stratigraphy, sedimentary sequence and the position of luminescence and**
350 **radiocarbon samples at Xiamabei. a**, Main stratigraphic column. **b**, Layers identified in the
351 field. **c**, Bayesian model of AMS ^{14}C and OSL dates. The age probability distribution in blue, red
352 and gray correspond to the OSL, AMS ^{14}C and modelled ages, respectively.

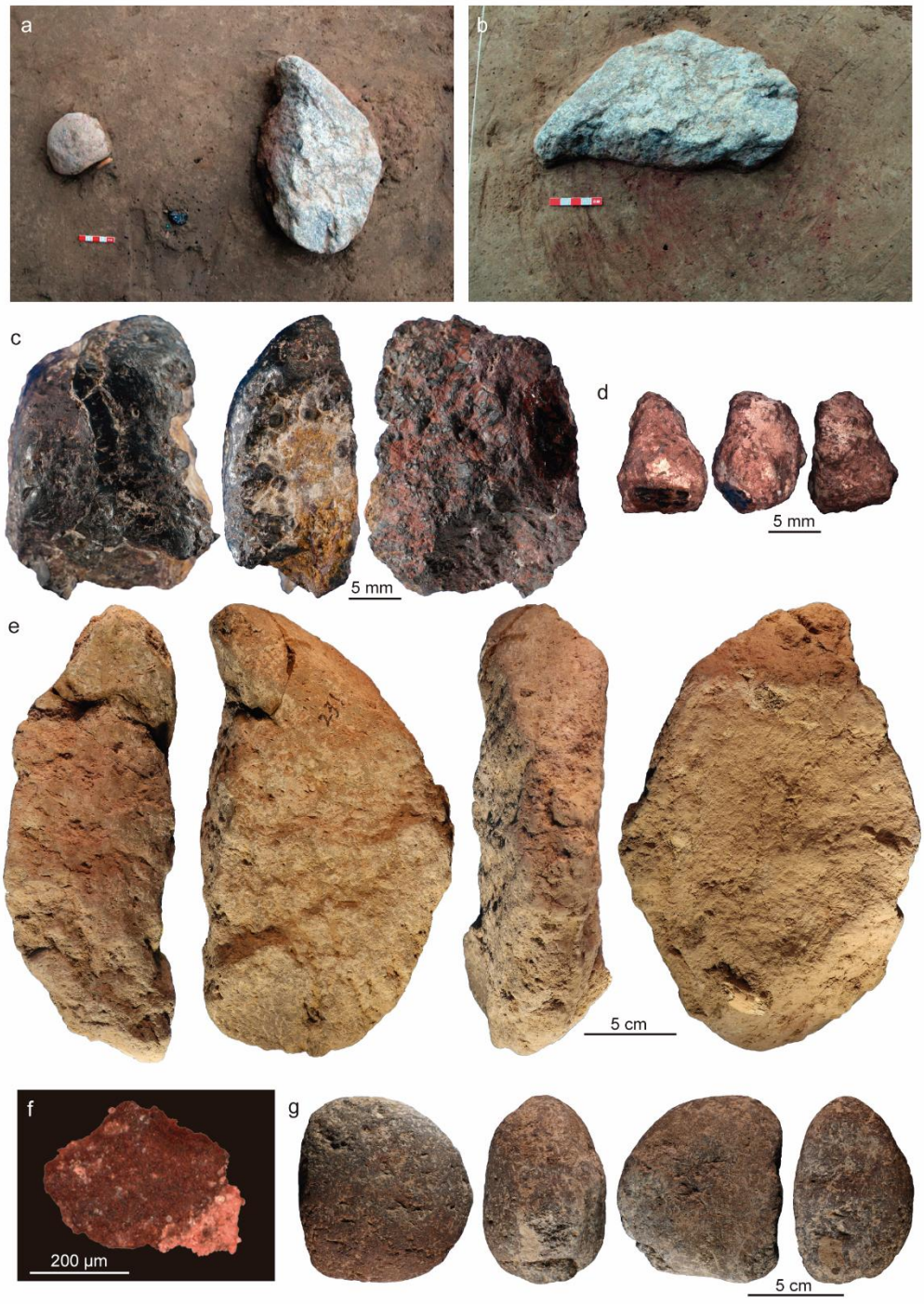

353

354 **Fig. 3 | Artefacts laying on the red stained sediment patch. a**, Quartzite cobble (QC),
355 limestone slab (LS) and ochre piece (OP1) identified during the excavation. **b**, LS laying on an
356 intense red stained sediment patch. **c**, Ochre piece modified by grinding (OP1). **d**, Ochre
357 fragment probably resulting from crushing a larger ochre piece (OP2). **e**, LS showing ochre
358 staining. **f**, Ochre microfragment (OMF) collected on the LS. **g**, Quartzite cobble (CG).

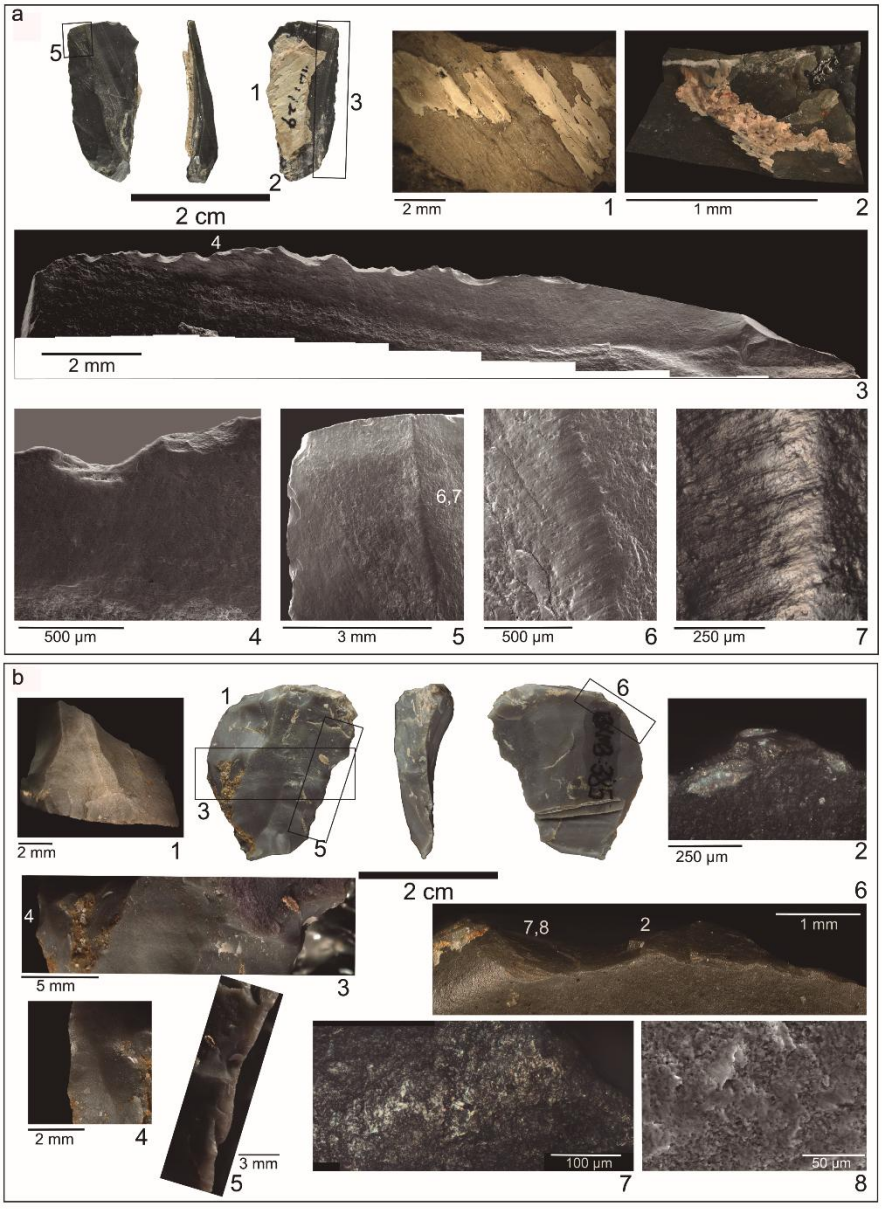

359

360 **Fig. 4 | Examples of use wear on lithics and residues on hafted pieces. a,** Bladelet-like piece
361 with an adhering portion of the bone haft (no. 129); (1) detail of the bone; (2) imprints of plant
362 fibers on calcium carbonate concretions likely related to binding; (3) ventral view of the active
363 edge; (4-7) several details of the grit-influenced plant polish produced by a whitling action. **b,**
364 End-scraper with punctual distal retouch (no. 385); (1) frontal view of the retouched area; (2)
365 spot with ochre particles on the active distal end; (3-5) scarring and slight adequation on the
366 hafted portion; (6-8) use wear produced by hide scraping. Images: a1-2 and b1, 3-6 3D Digital
367 Microscope; a3-6, b8 Scanning Electron Microscope; a7, b2, 7 Reflected Light Optical
368 Microscope.

Methods

Radiocarbon dating

Six animal bone fragments (all mammals) from Layers 2, 4 and 6 were collected and submitted to the Oxford Radiocarbon Accelerator Unit (ORAU) for radiocarbon dating. The bones were pretreated using routine methods for collagen extraction and purification, including an ultrafiltration step, as described in Ramsey et al.[34] and Brock et al.[34].

The dates are reported in radiocarbon years BP (Before Present - AD 1950) using the half-life of 5568 years. Isotopic fractionation was corrected for using the $\delta^{13}C$ values measured on the AMS. The quoted $\delta^{13}C$ values are measured independently on a stable isotope mass spectrometer (to ±0.3 per mil relative to VPDB). The new ^{14}C determinations are calibrated using the INTCAL20 calibration curve[36] and the OxCal 4.4 platform[37], with the age ranges in Supplementary Information Table C1 expressed at the 95.4% confidence interval. The dating report is included in Supplementary Information C1.

Luminescence dating

Dating of sediments using optically stimulated luminescence (OSL) signals in mineral grains was first introduced by Huntley et al.[38]. The OSL dating technique mostly determines the time elapsed since the last sunlight exposure of a deposit, i.e., its burial time. The technique has been widely used to date geological and archaeological deposits[39–42] in recent decades. The luminescence emitted from minerals (e.g., quartz and feldspar) under artificial light exposure is proportional to the absorbed energy accumulated within the crystal lattice of minerals by ionizing radiation (e.g., alpha, beta or gamma radiation) from radioactive elements such as uranium (U), thorium (Th), and potassium (K) in the environment, as well as cosmic rays[40,43]. The total luminescence of a sample which is often calibrated as a radiation dose (termed the equivalent dose, De), is determined by comparing natural luminescence signals with signals yielded after a known laboratory irradiation dose. Calculating the rate of natural irradiation (dose rate) at which the sample absorbs energy from radiation in the environment during burial involves assessing the radioactivity of the sample and its surroundings using chemical and radiometric methods, and estimating the radiation contributed by cosmic rays. The luminescence age of sediments is then

achieved by subdividing the equivalent dose (Gy) by the dose rate (Gy/ka)[44].

A total of 10 sediment samples (Supplementary Information Table C3) was collected in the Xiamabei sequence for OSL dating. All OSL samples were obtained by hammering steel tubes (20 cm-long cylinders with a diameter of 5 cm) into a freshly dug vertical section. The tubes were then covered and sealed with aluminum foil, and wrapped in black plastic bags and taped to avoid light exposure and moisture loss. The sediment from the sunlight-exposed end of the cylinder was separated and used for dose rate measurement. The material from the middle of the cylinder was used for De measurement. Sample preparation, measurement and data analysis procedures are described in Supplementary Information C2.

Bayesian modelling and age of the Xiamabei section

To establish the precise chronological framework of individual depositional units in Xiamabei, we conducted Bayesian analysis that includes both the optical and ^{14}C ages, using OxCal v4.4 [45–49]. All ^{14}C ages were calibrated using the INTCAL 20 calibration curve. For each OSL age, we used C date in calendar years before 2020 when the samples were collected with associated 1σ errors as likelihood estimates. In order to harmonise the time the OSL was obtained and the radiocarbon convention "BP=1950", we subtracted 70 years from the OSL ages (2020−1950) prior to them being modeled.

In order to estimate the posterior distributions (i.e., the modelled ages), the stratigraphic order of each sample was input using the Sequence function (Supplementary Information Table C4), based on the prior assumption that a sample stratigraphically lower is older than those above. Samples that are from the same stratigraphic layer with similar depth, such as in Layer 6, were modelled as a Phase, in which the measured ages are assumed to belong to same period. For the layers with abrupt and clear boundaries between them, such as Layers 6 and 5, double (upper or lower) boundaries were placed for them to constrain their start or end ages. Otherwise, for layers which gradual stratigraphic changes were identified, assuming continuous sediment accumulation, single transitional boundaries were placed between them. The samples, phases and sequences were arranged according to their relative stratigraphic order.

To check for outliers, we applied the general t-type outlier model to detect outlier ages by assessing the likelihood of each age being consistent with the modelled ages. A prior outlier probability of 5% was assigned for the other samples with their posterior outlier probability

calculated during the modelling process. The CQL codes used to run the Bayesian model and generate posterior age estimates are listed in Supplementary Information Table C5. The generated probability distribution functions (PDF) for each of the samples are shown in Fig. 2 and their corresponding 95.4% probability ranges are summarized in Supplementary Information Table C5. As demonstrated in Fig. 2, the Bayesian model results in a significant improvement of the precision in age estimates for all the samples. None of the samples was flagged as an outlier, as indicated by the posterior outlier probabilities, which are less than 4% for all samples. Using a Date command we calculated the total span of each phase of interest, in particular, Layer 6 and Layer 4. The model is shown in Supplementary Information C3.

Ochre analysis

Four artefacts were submitted to microscopic and geochemical analyses (Fig. 3): two ochre pieces (OP1 and OP2, Extended Data Figs. 2,3), a quartzite cobble (QC, Extended Data Fig. 4) and an elongated limestone slab (LS, Extended Data Fig. 5). During excavation, these four artefacts were found in close spatial association (Fig. 3a) and lying on a large red stained sediment spot (Fig. 3b). The cobble was cleaned under the microscope with a wet toothpick and a soft brush. The recovered sediment was analysed to check the presence of phytoliths (Supplementary Information F).

The four artefacts were examined with a motorised Leica Z6APOA microscope equipped with a DFC420 digital camera and Leica Application Suite software (v.4.13, Wetzlar, Germany), equipped with the Multifocus module and Leica Map DCM 3D computer software (6.2, Wetzlar, Germany). The Multifocus module allows the acquisition of extended depth of field images by relying on adapted algorithms that combine digital images collected at different heights into a single, sharp, composite image. The obtained microscopic images were digitized and edited in the Adobe® Photoshop® CS5.1 Extended software. The Leica Map DCM 3D allowed production of 3D reconstructions of areas of interest on OP1.

Anthropogenic modifications on grindstones and ochre pieces were identified macro- and microscopically. On grindstones, we recorded the presence of pits (depressions produced by a pounding action), and smoothed areas (surfaces that have lost, comparatively to neighbouring areas, irregularities and projections through abrasive action)[50–52]. On ochre pieces, we identified polished areas (shiny surfaces that may have been produced by use or by rubbing against a soft

surface), striations (linear parallel marks arranged in groups produced by grinding the piece against an abrasive surface), and facets (flat areas covered with striations produced by grinding an object on a flat, hard abrasive surface)[53–55].

An ochre microfragment (OMF, Fig. 3f; Extended Data Fig. 5) adhering to the surface of the limestone slab LS (zone 1 in Extended Data Fig. 5a) was removed with a scalpel under the microscope without producing any damage to the artefact and put on a carbon adhesive tab adhering to a SEM stub.

Scanning Electron Microscopy (SEM) observations and Energy Dispersive X-Ray spectroscopy (EDS) analyses on OP1 and OP2 were conducted with a JEOL IT 500 HR instrument equipped with two EDS Oxford Instruments Ultimax 100 spectrometers. Both samples were observed under the same magnifications (×60, ×1000, ×3000, ×4000 and in a few cases x10,000) (Supplementary Information E). EDS analyses and backscattered electron images (BSE) were obtained under low vacuum mode at a pressure of 30 Pa with a 20 kV accelerating voltage. SEM observations and EDS analyses on sample OMF were conducted with a Tescan Vega3 XMU scanning electron microscope (TESCAN FRANCE, Fuveau, France) equipped with an Oxford X-MaxN 50 EDS detector (Oxford Instruments, Abingdon, U.K). A 10 kV accelerating voltage was used for imaging using secondary and backscattered electrons, and 20 kV for EDS analyses. All samples were observed with no prior metal or carbon coating. All EDS spectra were processed with the Aztec software (version 3.1, Oxford Instruments, UK).

µ-Raman (µ-RS) analyses were conducted to determine the mineralogical composition of OP1, OP2 and sample OMF, using a SENTERRA Dispersive Raman Microscope (Bruker) equipped with an internal calibration system. The working area was examined using an integrated colour camera. Spectra were acquired with a 785 nm laser and a laser power of 1 to 10 mW. The spectra were recorded with an integration time varying from 5 to 10 s, in a spectral range from 100 to 2200 cm^{-1}, with a number of co-additions varying between 5 to 10 depending on the presence of fluorescence radiation and signal-to-noise ratio. Data was collected with the OPUS 7.2 software package (Bruker, Billerica, USA). Mineral identification was based on the comparison of the recorded spectra with those of available in the RRUFF spectra library, University of Arizona[56].

The elemental composition of OP1 and OP2 was established by energy dispersive X-ray fluorescence (EDXRF) (Extended Data Fig. 6). Measurements were acquired using a positioning

device consisting of a metallic receptacle to which the spectrometer was fixed. Sample OMF was not analysed because its size is smaller than the spectrometer aperture (3x4 mm in diameter)[57]. EDXRF measurements were performed with a portable SPECTRO xSORT X-ray fluorescence spectrometer from Ametek, equipped with a silicon drift detector (SDD), a W X-ray tube with an excitation source set at 40 kV, 0.1 mA. Spectra acquisition times were set to 120 s. The spectrometer is internally calibrated by an automated measure of the elemental composition of a standard metal shutter. A supplementary calibration[58,59], based on the Lucas-Tooth and Price methodology, was applied[60]. This calibration, developed with the X-labpro software (Ametek, Berwyn, USA) adjusts the mass attenuation coefficient and calibration slopes for major and trace elements by using certified standards and reference samples analysed by ICP-OES and ICP-MS. The Ochre analysis results in details can be found in Supplementary Information E.

Sediment analysis

Twelve sediment samples, as listed in Supplementary Information Table G1, were selected for mineralogical, elemental and magnetic analysis. Two samples (X1 and X2) come from the red stained area on which the ochre fragments OP1 and OPI2, limestone slab LS and cobble QS were found (Extended Data Fig. 10), two samples (X3 and X6) were retrieved in the same layer but at ca. 2 m far from the stained area, eight other (X4, X5, XMB2101−XMB2106) were collected between 20 and 200 m far from the excavated area (Supplementary Information Fig. G1). All the samples consist of floodplain silt.

XRD analysis[61] was carried out on the twelve samples (Supplementary Information Table G1), using a Netherland PANalytical X'PerPRO diffractometer with the following parameters: Ni-filtered Cu-Kα/40kV/40mA, scattering slit of 1/16°, receiving slit of 5 mm, continuous scan mode, scanning speed of 0.049884°/s, and a scanning step of 0.0167113°. Bulk minerals were identified based on the following peaks: quartz, 4.26 Å; anorthoclase, 3.21 Å; albite, 3.18 Å; rutile, 3.189 Å; calcite, 3.03 Å; dolomite, 2.89 Å; Hematite, 2.70 Å; Koninckite, 8.42 Å; and clay minerals smectite/chlorite, 14.1 Å; illite, 10.0 Å. The relative proportions of the identified minerals were roughly determined using their peak intensities by measuring the heights of the main reflections with PANalytical X'pert HighScore software (Version 2.2e).

Raman spectra[61,62] were obtained with a Witec alpha300R confocal-Raman spectrometer equipped with a solid-state continuous-wave laser emitting at 532 nm, and diffraction gratings of

300 grooves mm^{-1}. A piece of single-crystal silicon was used to calibrate the wavenumbers of the shifts. Laser focusing and sample viewing are performed through a Zeiss microscope fitted with an EC Epiplan 50× objective lens (NA=0.75). The spot size is less than 1 μm and the resolution is 4.8 cm^{-1}. The laser power impinging on the hematite single crystal was 0.40 mW. A spectra acquisition time of 30 s and total spectra with 20 accumulations were collected for each measurement.

Non-destructive Micro-XRF analyses were performed on the twelve sediment samples (Supplementary Information Table G1) following the procedures of Li et al.[63]. The Micro-XRF measurements were carried out on the M4 TORADO PLUS Micro-XRF analyzer. One area of about 0.5–1 cm^2 for each sample was randomly selected for collecting the XRF signals with the same measuring parameters (e.g., 50 kV of high voltage, 600 μA of anode current, 20 μm of spot size, 10 μm of pixel size, and 20 ms/pixel of pixel time). For semi-quantitative comparisons, each XRF spectrum was normalized with the signal of the Rh-La peak, which is generated by a Rh X-ray source. The data were analyzed with the M4 TORNADO Bruker Microanalysis Software.

Mineral magnetic measurements were made on the twelve sediment samples (Supplementary Information Table G1) in order to determine the magnetic mineralogy[64–71]. χ-T curves were obtained by continuous exposure of samples through temperature cycles from room temperature to 700°C and back to room temperature with a ramping rate of 2°C/min, using an AGICO MFK1-FA equipped with CS-3 temperature control system. To minimize the possibility of oxidation, the samples were heated and cooled in an argon atmosphere. For each sample, we subtracted the contribution of the sample holder and thermocouple to the magnetic susceptibility. Hysteresis loops were measured using a MicroMag 3900 Vibrating Sample Magnetometer (VSM) (Princeton Measurements Corp., USA). The magnetic field was cycled between ±1.5 T for each sample. Saturation magnetization (M_s), saturation remanence (M_r), and coercivity (B_c) were determined after the correction for the paramagnetic contribution identified from the slope at high fields. Samples were then demagnetized in alternating fields up to 1.5 T, and an isothermal remanent magnetization (IRM) was imparted from 0 to 1.5 T also using the MicroMag 3900 VSM. Subsequently the IRM at 1.5 T was demagnetized in a stepwise backfield from 0 to −1.5 T to obtain coercivity of remanence (B_{cr}). Magnetic component analyses of coercivity distributions were analyzed using the IRM-CLG program of Kruiver et al.[66].

549 To better constrain the origin and microstructure of the sediment, selected samples (X1, X2,
550 X4, X6) were observed using optical microscopy and analysed using Scanning Electron
551 Microscopy (SEM) coupled with Energy Dispersive X-Ray spectroscopy (EDS). Backscattered
552 electron microscopy analyses were conducted using a scanning electron microscope with an
553 energy dispersive spectrometer (JSM-IT500).
554 Detailed results of the sediment analyses can be found in Supplementary Information G.
555

556 **Stone tool functional and residue analysis**

557 The stone tool functional analysis is based on the fundamentals of traceology[72–74], which has
558 been subsequently consolidated, systematized[75–79] and strengthened to improve interpretion[76,77].
559 The study applied criteria established experimentally[80–84], incorporating a multi-scalar approach
560 and a multi-technique microscopic analysis[75–88]. Potential residues were characterized
561 microscopically, including study of their elementary chemical composition, without removing
562 adhering materials from tools[89–92].
563 Use-wear and residues were documented with the combined use of Optical Microscopy
564 (OM), Scanning Electron Microscopy (SEM) and 3D Digital Microscopy (3D DM). Four main
565 procedures (I-IV) were used for analysis.
566 I) A preliminary assessment of the samples and the location of features of special interest
567 was conducted. This was conducted at low magnification, using a stereomicroscope (Euromex
568 DZ.1105), with a magnification range of 8×-80× (0.8×-8× zoom, 10× oculars), and equipped
569 with a 20MP 1” Scemex camera (Horizontal Field of View 16.6 mm -1.67 mm).
570 II) A systematic screening at different magnifications using 3D DM (Hirox KH-8700) was
571 conducted. This microscope is equipped with a dual illumination revolver zoom lens (MXG-
572 5000REZ) which together with the high intensity LED light source allows for the observation of
573 samples with a 5700 K color temperature. This lens consists of a triple objective turret with a
574 different zoom range per objective, allowing for magnifications ranging from 35 to 5000×
575 (HFOV 8.6 mm–60 μ). The microscope is equipped with a high-sensitivity compact CCD camera
576 that enabled the capture of 24 frames per second at high resolution (1600×1200 pixels). The dual
577 illumination system allows for the observation of sample topography with ring and coaxial light.

The former is suitable for the observation of topographical irregularities with a uniform even illumination at low magnifications, while coaxial light serves to highlight the topography of flat surfaces at high magnifications. Ring and coaxial lights were used individually and even combined, according to the observation conditions required by the samples. The interest of this microscope lies on its integrated stacking and stitching technology, capable of performing real-time 2D and 3D tiltings and generating wide field of view images of large surface areas which, in turn, create quantifiable 3D models.

III) More conventional observations were conducted with a reflected light microscope. We used a Zeiss Axio Scope A.1 metallographic microscope, with differential interference contrast (DIC) system involving a Nomarsky interference contrast filter. The microscope was equipped with 10× oculars and objectives EC Epiplan ranging from 5×/0.13 to 50×/0.5 HD DIC, resulting in nominal magnifications ranging from 50 to 500 times. Pictures were taken with a 6.3 MP 1.8" FLIR camera, and fully focused images were obtained through a motorized stage and Winkoms Encoder Z 1.0 and Helicon Focus 5.3 software. Resulting HFOV ranges from 2.9mm to 295µm.

IV) An environmental SEM (ESEM FEI Quanta 600 model) with an energy dispersive X-ray spectrometer (EDX-EXL II System analytical oxford) for microanalysis, equipped with an INCA software (v 4.01) from Oxford Instruments for digital image acquisition, was conducted. Most observations were carried out between 60× and 2000× (HFOV 6.9 mm to 207 µ, 24" display). Observations were entirely done in low vacuum mode (LV), so the coating of the samples with conductive materials (gold or carbon) was not required. Large field (LFD) and back-scattered electron detectors (DualBSD) were used in combination to observe residues and use-wear features.

Sample processing based on protocols tested in previous studies[79,87] were adapted in our microscopic workflow. No cleaning was applied during first observations; a very soft cleaning was performed prior to the characterization of residues by OM, 3D DM or SEM analysis; and, a more thorough cleaning was subsequently applied when necessary, to document use-wear features in detail. The main cleaning steps were: 1) Removal of the ink and varnish used to mark the archaeological tools with acetone; 2) 5 to 15 min ultrasonic baths in a 2% neutral phosphate-free detergent solution (Derquim®); 3) 5 min baths in hydrogen peroxide (H_2O_2, 130vol) to remove modern organic matter, when spotted; 4) Removal of residues from cleaning products under running water; 5) 2–5 min ultrasonic baths in pure acetone to remove any residues from

handling. When necessary, 5 min baths in a 10% HCl solution were applied to remove carbonated residues. Before each observation, tools were dried with compressed air to avoid contact with the laboratory paper and to reduce the formation of liquid spots on the surface, which may lead to misleading interpretations. During the entire process, samples were handled using powder-free gloves and plastic tweezers.

Experimental reference collections available at the IPHES Lithic Technology Laboratory, derived from published and ongoing programs, were used to compare to the Xiamabei results, thereby assisting in interpretations. The experimental programs involved actions on a range of common contact materials, and artefacts made on a variety of raw materials, including chert, quartzite, quartz, limestone, basalt, and obsidian[83–85,88,90,91,93–97]. Interpretations were also supported by information supplied in the wider literature. Detailed reporting on the Xiamabei samples is provided in Supplementary Information I.

34. Ramsey, B. C., Higham, T. & Leach P. Towards high-precision AMS: Progress and limitations. *Radiocarbon* **46**, 17–24 (2004).
35. Brock, F., Higham, T., Ditchfield, P. & Ramsey C. B. Current pretreatment methods for AMS radiocarbon dating at the Oxford Radiocarbon Accelerator Unit (ORAU). *Radiocarbon* **52**, 103–112 (2010).
36. Reimer, P. et al. The IntCal20 Northern Hemisphere radiocarbon age calibration curve (0–55 cal kBP). *Radiocarbon* **62**, 725–757 (2020).
37. Bronk, C. B. Bayesian analysis of radiocarbon dates. *Radiocarbon* **51**, 337−360 (2009).
38. Huntley, D. J., Godfrey-Smith, D. I. & Thewalt, M. L. W. Optical dating of sediments. *Nature* **313**, 105–107 (1985).
39. Duller, G. Distinguishing quartz and feldspar in single grain luminescence measurements. *Radiat. Meas.* **37**, 161–165 (2003).
40. Rhodes, E. J. Optically stimulated luminescence dating of sediments over the past 200,000 years. *Annu. Rev. Earth Planet. Sci.* **39**, 461–488 (2011).
41. Zhang, X. L. et al. The earliest human occupation of the high-altitude Tibetan Plateau 40 thousand to 30 thousand years ago. *Science* **362**, 1049–1051 (2018).
42. Ge, J. Y. et al. Evidence from the Dayao Palaeolithic site, Inner Mongolia for human migration into arid northwest China during mid-Pleistocene interglacials. *Quat. Res.* **103**, 113–129.
43. Duller, G. Luminescence dating of Quaternary sediments: Recent advances. *J. Quat. Sci.* **19**, 183–192 (2004).
44. Aitken, M. J. *Introduction to Optical Dating: The Dating of Quaternary Sediments by the Use of Photon-Stimulated Luminescence* (Clarendon Press, 1998).
45. Ramsey, B. C. Deposition models for chronological records. *Quat. Sci. Rev.* **27**, 42–60 (2008).
46. Ramsey, B. C. Bayesian analysis of radiocarbon dates. *Radiocarbon* **51**, 337–360 (2009).
47. Ramsey, B. C. Dealing with outliers and offsets in radiocarbon dating. *Radiocarbon* **51**, 1023–1045 (2009).
48. Ramsey, B. C. *Bayesian Approaches to the Building of Archaeological Chronologies* (CRC Press Boca Raton, FL, 2015).
49. Ramsey, B. C. Methods for summarizing radiocarbon datasets. *Radiocarbon* **59**, 1809–1833 (2017).
50. Adams, J. et al. “Functional analysis of macro-lithic artefacts” in Non-Flint Raw Material Use in Prehistory: Old Prejudices and New Directions, F. Sternke, L. Eigeland, L.J. Costa, Eds. (Archaeopress,

2009), pp. 43–66.
51. de Beaune, S. *Pour une archéologie du geste: Broyer, moudre, piler, des premiers chasseurs aux premiers agriculteurs* (CNRS Editions, 2000).
52. Rosso, D. E., Mart, í A. P. & d' Errico, F. Middle Stone Age ochre processing and behavioural complexity in the Horn of Africa: Evidence from Porc-Epic Cave, Dire Dawa, Ethiopia. *PLoS ONE* **11**, e0164793 (2016).
53. Hodgskiss, T. Identifying grinding, scoring and rubbing use-wear on experimental ochre pieces. *J. Archaeol. Sci.* **37**, 3344–3358 (2010).
54. Rifkin, R. F. Processing ochre in the Middle Stone Age: Testing the inference of prehistoric behaviours from actualistically derived experimental data. *J. Anthropol. Archaeol.* **31**, 174–195 (2012).
55. Rosso, D. E., d'Errico, F. & Queffelec, A. Patterns of change and continuity in ochre use during the late Middle Stone Age of the Horn of Africa: the Porc-Epic Cave record. *PLoS ONE* **12**, e0177298 (2017).
56. Lafuente, B., Downs, R. T., Yang, H. & Stone N. "The power of databases: the RRUFF project" in Highlights in Mineralogical Crystallography, T. Armbruster, R. M. Danisi, Eds. (W. De Gruyter, 2015) pp. 1–30.
57. Bassel, L. et al. Fluorescence-based knife-edge beam diameter measurement to characterize X-ray beam profiles in reflection geometry. *Spectroc. Acta Pt. B-Atom. Spectr.* **118**, 98–101 (2016).
58. Dayet, L. et al. Manganese and iron oxide use at Combe-Grenal (Dordogne, France): A proxy for cultural change in Neanderthal communities. *J. Archaeol. Sci. Rep.* **25**, 239–256 (2019).
59. Queffelec, A., d'Errico, F.& Vanhaeren, M. "Analyse des blocs de matière colorante de Praileaitz I (Deba, Gipuzkoa)" in Munibe Monographs (Anthropology and Archaeology Series, 2017). pp. 493–503.
60. Lucas-Tooth, H. J. and Price, B. J. A mathematical method for the investigation of inter-element effects in X-ray fluorescence. *Metallurgia* **64**, 149–152 (1961).
61. Anthony, J. W., Bideaux, R. A., Bladh, K. W. & Nichols, M. C. *Handbook of Mineralogy* (Mineral Data Publishing, Tucson Arizona, USA, 1990).
62. Hanesch, M. Raman spectroscopy of iron oxides and (oxy)hydroxides at low laser power and possible applications in environmental magnetic studies. *Geophys. J. Int.* **17**, 941–948 (2009).
63. Li, J. H. et al. Micro-XRF study of the troodontid dinosaur *Jianianhualong Tengi* reveals new biological and taphonomical signals. *Atomic Spectroscopy* **42**, 1–11 (2021).
64. Deng, C., Zhu, R., Jackson, M. J., Verosub, K. L. & Singer, M. J. Variability of the temperature-dependent susceptibility of the Holocene eolian deposits in the Chinese loess plateau: a pedogenesis indicator. *Phys. Chem. Earth (A)* **26**, 873–878 (2001).
65. Dunlop, D. J. & Özdemir Ö. *Rock Magnetism: Fundamentals and Frontiers* (Cambridge Univ. Press, Cambridge, UK, 1997).
66. Kruiver, P. P., Dekkers, M. J. & Heslop, D. Quantification of magnetic coercivity components by the analysis of acquisition curves of isothermal remanent magnetization. *Earth Planet. Sci. Lett.* **189**, 269–276 (2001).
67. Jiang, Z. et al. Ferro and antiferromagnetism of ultrafine-grained hematite. *Geochem. Geophys. Geosyst.* **15**, 2699–2712 (2014).
68. Özdemir, Ö. & Dunlop, D. J. Hysteresis and coercivity of hematite. *J. Geophys. Res. Solid Earth* **119**, 2582–2594 (2014).
69. Roberts, A. P., Cui, Y. & Verosub, K. L. Wasp-waisted hysteresis loops: mineral magnetic characteristics and discrimination of components in mixed magnetic systems. *J. Geophys. Res.* **100**, 17909–17924 (1995).
70. Yuan, J. et al. Rapid drift of the Tethyan Himalaya terrane before two-stage India-Asia collision. *Natl. Sci. Rev.* **8**, nwaa173, doi:10.1093/nsr/nwaa173 (2021).
71. Roberts, A. P. et al. Hematite (α- Fe_2O_3) quantification in sedimentary magnetism: limitations of existing proxies and ways forward. *Geosci. Lett.* **7**, 8, doi:10.1186/s40562-020-00157-5 (2020).
72. Semenov, S. A. *Prehistoric Technology. An Experimental Study of the Oldest Tools and Artefacts From Traces of Manufacture and Wear* (Cory, Adams and Mackay Ltd., London, 1964).
73. Hayden, B. (Ed), *Lithic Use-Wear Analysis* (Academic Press, New York, 1979).
74. Keeley, L. H. *Experimental Determination of Stone Tools Uses: A Microwear Analysis* (The University of Chicago Press, Chicago, 1980).
75. Vaughan, P. C. *Use-Wear Analysis of Flaked Stone Tools* (The University of Arizona Press, Tucson, 1985).

76. Knutsson, K. Patterns of tools use. Scanning electron microscopy of experimental quartz tools (Societas Archaeologica Upsalensis, Uppsala, 1988), vol. 10.
77. González, J. E. & Ibáñez, J. J. *Metodología de Análisis funcional de instrumentos tallados en sílex* (Universidad de Deusto, Bilbao, 1994)
78. Levi Sala, I. *A Study of Microscopic Polish on Flint Implements* (Tempus Reparatum, Oxford, 1996). BAR IS629.
79. Marreiros, J. M., Gibaja Bao, J. F. & Ferreira Bicho, N. *Use-Wear and Residue Analysis in Archaeology* (Springer Cham Heidelberg New York, 2015).
80. Stemp W. J., Watson A. S. & Evans A. A. Surface analysis of stone and bone tools. *Surf. Topogr. Metrol. Prop.* **4**, 13001 (2016).
81. Ollé, A. & Vergès, J. M. "SEM functional analysis and the mechanism of microwear formation" in 'Prehistoric Technology' 40 years later: Functional Studies and the Russian Legacy. Proceedings of the International Congress Verona (Italy), 20-23 April 2005, Longo L., Skakun N., Eds. (Archaeopress, Oxford, 2008), BAR 1783, pp. 39–49.
82. Ollé, A. & Vergès, J. M. The use of sequential experiments and SEM in documenting stone tool microwear. *J. Archaeol. Sci.* **48**, 60–72 (2014).
83. Fernández-Marchena, J. L. & Ollé, A. Microscopic analysis of technical and functional traces as a method for the use-wear analysis of rock crystal tools. *Quat. Int.* **424**, 171–190 (2016).
84. Pedergnana, A. & Ollé, A. Monitoring and interpreting the use-wear formation processes on quartzite flakes through sequential experiments. *Quat. Int.* **427**, 35–65 (2017).
85. Borel, A., Ollé, A., Vergès, J. M. & Sala, R. Scanning Electron and Optical Light Microscopy: two complementary approaches for the understanding and interpretation of usewear and residues on stone tools. *J. Archaeol. Sci.* **48**, 46–59 (2014).
86. Ollé, A. et al. Microwear features on vein quartz, rock crystal and quartzite: a study combining Optical Light and Scanning Electron Microscopy. *Quat. Int.* **424**, 154–170 (2016).
87. Pedergnana, A., Ollé, A. & Evans, A. A. A new combined approach using confocal and scanning electron microscopy to image surface modifications on quartzite. *J. Archaeol. Sci. Rep.* **30**, 102237 (2020).
88. Martín-Viveros, J. I. & Ollé, A. Use-wear and residue mapping on experimental chert tools. A multi-scalar approach combining digital 3D, optical, and scanning electron microscopy. *J. Archaeol. Sci. Rep.* **30**, 102236 (2020).
89. Monnier, F., Ladwig, J. & Porter, L. S. T. Swept under the rug: the problem of unacknowledged ambiguity in lithic residue identification. *J. Archaeol. Sci.* **39**, 3284–3300 (2012).
90. Pedergnana, A., Asryan, L., Fernández-Marchena, J. L. & Ollé, A. Modern contaminants affecting microscopic residue analysis on stone tools: A word of caution. *Micron* **86**, 1–21 (2016).
91. Pedergnana, A. & Ollé, A. Building an experimental comparative reference collection for lithic micro-residue analysis based on a multi-analytical approach. *J. Archaeol. Method Theory* **25**, 117–154 (2018).
92. Xhauflair, H. et al. Use-related or contamination? Residue and use-wear mapping on stone tools used for experimental processing of plants from Southeast Asia. *Quat. Int.* **427**, 80–93 (2017).
93. Martín-Viveros, J. I. & Ollé, A. Using 3D digital microscopy and SEM-EDX for in-situ residue analysis: A multi-analytical contextual approach on experimental stone tools. *Quat. Int.* **569–570**, 228–262 (2020).
94. Hayes, E., Cnuts, D. & Rots, V. Integrating SEM-EDS in a sequential residue analysis protocol: Benefits and challenges. *J. Archaeol. Sci. Rep.* **23**, 116–126 (2019).
95. Ollé, A. Variabilitat i patrons funcionals en els sistemes tècnics de Mode 2. Anàlisi de les deformacions d'ús en els conjunts lítics del Riparo Esterno de Grotta Paglicci (Rignano Garganico, Foggia), Áridos (Arganda, Madrid) i Galería-TN (Sierra de Atapuerca, Burgos). Thesis, Universitat Rovira i Virgili, Tarragona (2003).
96. Fernández-Marchena, J. L. et al. Rainbow in the dark. The identification of diagnostic projectile impact features on rock crystal. *J. Archaeol. Sci. Rep.* **31**, 102315 (2020).
97. Martín-Viveros, J. I. et al. Use-wear analysis of a specific mobile toolkit from the Middle Palaeolithic site of Abric Romaní (Barcelona, Spain): a case study from level M. *Archaeol. Anthropol. Sci.* **12**, 16 (2020).
98. Downs, R.T. The RRUFF Project: an integrated study of the chemistry, crystallography, Raman and infrared spectroscopy of minerals. Program and Abstracts of the 19th General Meeting of the International Mineralogical Association in Kobe, Japan. p. 3–13. (2006).

99. Robertson, D. J. & France, D. E. Discrimination of remanence-carrying minerals in mixtures, using isothermal remanent magnetisation acquisition curves. *Phys. Earth Planet. Inter.* **82**, 223–234 (1994).
100. Swanson-Hysell, N. L., Fairchild, L. M. & Slotznick, S. P. Primary and secondary red bed magnetization constrained by fluvial intraclasts. *J. Geophys. Res. Solid Earth* **124**, 4276–4289 (2019).